Suppression of bacterial rheotaxis in wavy channels

Winfried Schmidt [1,2] Igor S. Aranson [3] and Walter Zimmermann [1,*]

[1]*Theoretische Physik, Universität Bayreuth, 95440 Bayreuth, Germany*

[2]*Université Grenoble Alpes, CNRS, LIPhy, F-38000 Grenoble, France*

[3]*Departments of Biomedical Engineering, Chemistry, and Mathematics, Pennsylvania State University, University Park, Pennsylvania 16802, USA*

Controlling the swimming behavior of bacteria is crucial, for example, to prevent contamination of ducts and catheters. We show that bacteria modeled by deformable microswimmers can accumulate in flows through straight microchannels either in their center or on previously unknown attractors near the channel walls. In flows through wavy microchannels we predict a resonance effect for semiflexible microswimmers. As a result, microswimmers can be deflected in a controlled manner so that they swim in modulated channels distributed over the channel cross section rather than localized near the wall or the channel center. Thus, depending on the flow amplitude, both upstream orientation of swimmers and their accumulation at the boundaries, which can promote surface rheotaxis, are suppressed. Our results suggest strategies for controlling the behavior of live and synthetic swimmers in microchannels.

I. INTRODUCTION

Bacteria are among the most widespread microorganisms in nature. One of the remarkable properties of motile bacteria is the ability to reorient their bodies against the flow and swim upstream, i.e., positive rheotaxis [1–3]. This often detrimental behavior leads to contamination of ducts and catheters that may lead to bacterial infections [4,5]. Positive rheotaxis occurs for sperm cells and plays an important role in the reproduction process [6–10]. Recently, rheotaxislike behavior was observed for synthetic self-propelled particles, although the mechanisms are not necessarily similar to that of bacteria and sperm cells [11–16]. Despite the importance of rheotaxis for human and animal health and reproduction, many underlying mechanisms are not clear.

The familiar dynamics of a rigid microswimmer in a planar Poiseuille flow are determined by the interplay between the swimmer's speed and the flow vorticity [3,17–19]. Two different types of motion have been identified. (i) The swinging motion is characterized by sinusoidal swimmer trajectories around the channel center. It occurs for small flow strengths compared to the swimming speed and in the vicinity of the channel center. (ii) The tumbling motion is observed for larger flow velocities and in regions away from the channel center where the flow vorticity is sufficiently strong to reorient the swimmer before it reaches the channel center, resulting in complete rotations of the swimmer.

Many microswimmers are deformable. They, for instance, bend their bodies [20,21] for the purpose of self-propulsion,

as in the case of *Spiroplasma* [22], or have flexible flagella [23–25]. Flexible elongated microswimmers migrate transversely to streamlines in plane Poiseuille flow [23,24], similar to semiflexible polymers [26,27], vesicles [28], droplets [29], or capsules in oscillating shear flows [30]. Semiflexible microswimmers can migrate across streamlines toward the channel center where they reorient against the flow [23,24], as shown in Fig. 1(a). This type of rheotaxis can result in swimmer accumulation at the channel center. We find two additional attractors for semiflexible microswimmers which are located near the plane channel walls and exist for large flow strengths compared to the swimmer's speed. The position of the associated repellers, separating inward and outward migration directions, depends on the flow velocity. In wavy Poiseuille flows [outlined in Fig. 1(b)] we find a resonance for certain flow strengths and channel geometries, resulting in the depletion of swinging swimmers from the channel center in a controlled manner. Furthermore, for large flow velocities, we report on a wavy-induced tumbling motion of swimmers which helps to suppress their migration to the peripheral attractors.

Our model for the microswimmer and the wavy flow is described in Sec. II. We then first focus on the swimmer behavior in unbounded plane Poiseuille flows in Sec. III and continue our analysis for the swimmer in unbounded wavy flows in Sec. IV. We then investigate the swimmer's behavior in both plane and wavy flows by taking into account the effects of the channel wall via a repulsive wall potential in Sec. V and discuss our findings in Sec. VI.

II. MODEL

A semiflexible microswimmer in a Newtonian fluid with viscosity η is modeled by N small spheres with radius a at positions $\mathbf{r}_i = (x_i, y_i, z_i)$ $(i = 1, \ldots, N)$, together with a

---

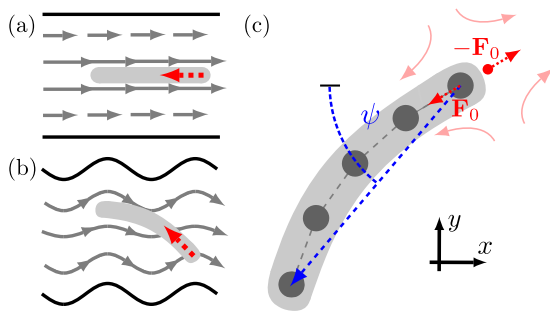*Corresponding author: walter.zimmermann@uni-bayreuth.de

FIG. 1. (a) Flexible swimmer (light gray, swimmer size enhanced) swims against the flow at the center of a plane channel or migrates towards the walls (not shown). Driving direction indicated by the red dashed arrow; channel walls are black lines. (b) A wavy channel suppresses this rheotaxis. (c) Deformable swimmer (light gray), composed of $N = 5$ beads (dark gray) in the x-y plane, with its mean orientation angle ψ (blue dashed line). The force dipole at its rear (pair of red arrows) creates a pusher-type flow field (light red dotted arrows) and thrust along the instantaneous driving direction, given by $\mathbf{F}_0$.

propelling force dipole at one end, as sketched in Fig. 1(c). $\mathbf{r}_c = \sum_{i=1}^{N} \mathbf{r}_i / N$ is the swimmer's center. The undeformed microswimmer has a straight shape with length $L_0 = (N-1)b + 2a$, where b is the equilibrium distance between two neighboring beads. The equations for the translational $\dot{\mathbf{r}}_i$ and angular velocities $\boldsymbol{\Omega}_i$ of each bead are given by

$$\dot{\mathbf{r}}_i = \mathbf{u}(\mathbf{r}_i) + \sum_{j=1}^{N+1} \boldsymbol{\mu}_{ij}^{\mathrm{tt}} \cdot \mathbf{F}_j + \sum_{j=1}^{N} \boldsymbol{\mu}_{ij}^{\mathrm{tr}} \cdot \mathbf{T}_j, \tag{1a}$$

$$\boldsymbol{\Omega}_i = \frac{1}{2} \nabla \times \mathbf{u}(\mathbf{r}_i) + \sum_{j=1}^{N+1} \boldsymbol{\mu}_{ij}^{\mathrm{rt}} \cdot \mathbf{F}_j + \sum_{j=1}^{N} \boldsymbol{\mu}_{ij}^{\mathrm{rr}} \cdot \mathbf{T}_j, \tag{1b}$$

with the mobility matrices $\boldsymbol{\mu}_{ij}^{lm}$ given in Appendix A and in Refs. [31,32]. $\mathbf{T}_i$ is the torque acting on the ith bead, cf. Eq. (A8), and $\mathbf{u}(\mathbf{r}_i)$ is the undisturbed background flow as described below. The force acting on the ith bead is $\mathbf{F}_i = -\nabla_i(V_i^{\mathrm{H}} + V_i^{\mathrm{B}})$, where V_i^{H} is a harmonic spring potential with spring constant k between neighboring beads. $V_i^{\mathrm{B}} = -\kappa/2 \ln(1 - \cos\alpha_i)$ is a bending potential [33] with bending rigidity κ and opening angle α_i of the chain at sphere i. V_i^{B} is minimal for $\alpha_i = \pi$, accounting for the straight undeformed shape. We assume an inextensible swimmer with large k and small κ to allow for bending.

There are different modeling approaches for elongated autonomous microswimmers [34,35]. Here, we employ in Eqs. (1) the mobility matrices for differently sized beads, as previously done for microswimmers driven by active springs [36]. Self-propulsion of our active bead-spring model is implemented via a driving force $\mathbf{F}_0 = F_0 \hat{\mathbf{e}}_s$ which acts on the Nth bead in the chain. Here, F_0 is the activity and $\hat{\mathbf{e}}_s := (\mathbf{r}_{N-1} - \mathbf{r}_N)/|\mathbf{r}_{N-1} - \mathbf{r}_N|$ the unit vector in driving direction. This force is balanced by its antiparallel counterpart $\mathbf{F}_p = -\mathbf{F}_0$, acting on a counterforce point which is located at $\mathbf{r}_p = \mathbf{r}_N - 2a\hat{\mathbf{e}}_s$. The flow disturbance caused by the counterforce point accounts for the $N + 1$st contribution to the translational and angular velocities in Eqs. (1); see Appendix A. With this,

we model an active drive (e.g., bacterial flagella) and a passive cargo (swimmer body). The active force $\mathbf{F}_0$ propagates via the springs from bead N to the other beads in the chain. The sum of all forces acting on the microswimmer is zero at any time, a hallmark of autonomous microswimmers. As a result, the created flow field decays with the inverse squared distance far away from the swimmer (see Appendix D). For $F_0 > 0$ the two opposite forces push the bacterial body in front of them and create a flow disturbance resembling a pusher-type flow field, whereas for $F_0 < 0$ they drag the body behind and a flow field similar to the one of a puller is created [37,38]. The swimming speed v_0 depends linearly on F_0 as shown in Appendix C, Fig. 9. Further validation of the model is given in Appendixes B and E. For simplicity, we restrict our analysis to the x-y plane and on pushers, as for rod-shaped swimmers like the bacteria *E. coli* or *B. subtilis*. The swimmer dynamics is characterized by the angle ψ between its end-to-end vector and the x axis. Pushers and pullers behave similarly for large parameter ranges.

We consider a serpentine channel geometry with equal modulation wavelength λ and phase for the two opposite walls [cf. Fig. 1(b)], which are located at

$$y_{\mathrm{w}}(x) = d\left[\pm 1 + \varepsilon \sin\left(\frac{2\pi x}{\lambda}\right)\right]. \tag{2}$$

Here, d is the channel half height and ε is the dimensionless modulation amplitude. That is in contrast to channels in Ref. [39] on cross-stream migration (CSM) of capsules and red blood cells, where modulations of the opposite walls are shifted by half a wavelength. For $\varepsilon \ll 1$, we determine the wavy flow field $\mathbf{u}(\mathbf{r}) = (u_x, u_y, 0)$ by a perturbation expansion,

$$u_x(x, y) = u_0\left[1 - \frac{y^2}{d^2} + \varepsilon U_1(x, y)\right], \tag{3a}$$

$$u_y(x, y) = u_0 \varepsilon U_2(x, y), \tag{3b}$$

with flow amplitude u_0. The functions $U_1(x, y)$ and $U_2(x, y)$ are given in Appendix F, Eqs. (F19) and the parameters in [40].

III. UNBOUNDED PLANE POISEUILLE FLOW

In this section, we analyze the swimmer behavior in unbounded plane Poiseuille flow, which is obtained for $\varepsilon = 0$ by Eqs. (3). Here, a rigid swimmer is described by a Hamiltonian system with periodic phase-space orbits that depend on the initial conditions [17,18]. A semiflexible microswimmer breaks the periodicity of its trajectory. For an initially tumbling swimmer, this causes an inward drift, i.e., cross-stream migration (CSM) towards the channel center, in addition to its motion along the streamlines. Once it reaches a critical distance to the channel center, the flow vorticity is not strong enough anymore to reorient the swimmer completely, and it transitions to a swinging motion with decaying amplitude [23,24], as shown in the bottom left panel of Fig. 2 (for the phase space trajectory, see Appendix E). The resulting swimmer reorientation against the flow, as sketched in Fig. 1(a), is thus caused by an interplay of its shear-flow induced deformation and self-propulsion F_0. This inward
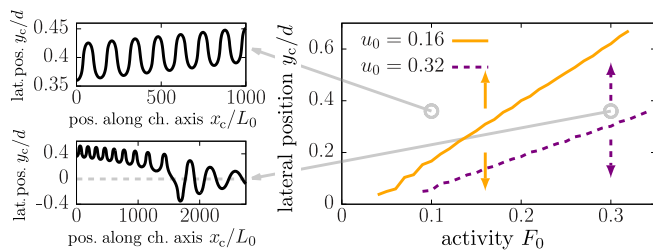
FIG. 2. Cross-stream migration of a semiflexible microswimmer in unbounded planar Poiseuille flow during tumbling. The channel center is at $y = 0$ (see gray dashed line) and no interactions with the channel walls are included. Two trajectories are shown for $u_0 = 0.16$ and $y_{c,0} = 0.36d$, with $F_0 = 0.1$ (top left) and $F_0 = 0.3$ (bottom left). In the first case, the swimmer migrates away from the channel center. In the second case, it migrates towards the center, transitions to swinging, and finally approaches a state of upstream orientation at the channel center. Right: a repeller separates these two types of trajectories, as shown for $u_0 = 0.16$ (orange bold line) and $u_0 = 0.32$ (violet dashed line). Arrows indicate the migration direction.

drift stands in contrast to the outward migration of passive soft particles with elongated shapes, such as flexible fibers and elongated vesicles [26,27]. This type of migration originates from the particle's hydrodynamic self-interaction and its shear-rate-induced deformation and is reproduced by us for slow swimmers; see top left panel of Fig. 2. These two competing migration mechanisms result in a repeller, as shown for two flow strengths in Fig. 2 (right), which separates outward- and inward-directed trajectories. This means that swimmers located outside of the repeller migrate further away from the channel center, while swimmers located inside of it migrate towards the center. The outward migration amplifies with the local shear rate, which in turn grows linearly with the distance from the channel center. Therefore, the mechanism of passive CSM dominates for small F_0 and large distances from the channel center, whereas the activity-induced inward CSM outweighs the outward CSM for growing F_0. This explains the shift of the repeller away from the channel center for increasing activity. The repeller for $u_0 = 0.16$ lies above the repeller for $u_0 = 0.32$, since weaker flows result in a larger relative influence of activity. We emphasize that during CSM swimmers always tumble. Whereas swinging takes place only for swimmers located on the inner side of the repeller with a sufficiently small distance to the channel center, swimmers beyond the repeller never transition to swinging. The $\pm y$ symmetry of a plane channel results in a second repeller in the lower channel half.

IV. UNBOUNDED WAVY POISEUILLE FLOW

In this section, we investigate the effects of wavy streamlines on the behavior of our semiflexible microswimmer by focusing on the range of small flow velocities compared to the swimmer's speed. The repellers in straight flows are then far away from the channel center and the activity-driven inward migration dominates for the swimmer. The swimmer trajectories in Fig. 3(a) illustrate characteristic differences in unbounded planar and wavy Poiseuille flow where $\varepsilon = 0.1$. In plane Poiseuille flow the swimmer first tumbles, then
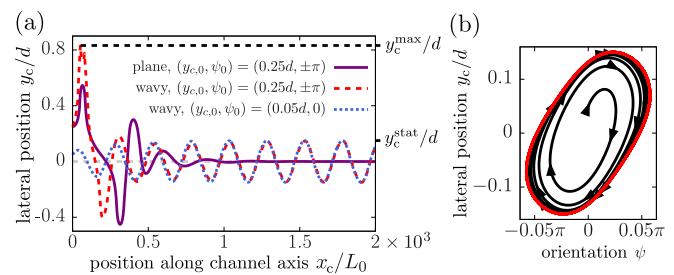

FIG. 3. (a) Comparison of real space trajectories of a semiflexible microswimmer with $F_0 = 0.6$ and $\kappa = 0.5$ in unbounded plane and wavy flows. The fixed point of upstream orientation at the center of a plane channel ($y = 0$, gray dashed line), adapted by the violet bold trajectory, is in a wavy flow replaced by a limit cycle (red dashed and blue dotted lines). The maximal (y_c^{max}) and steady-state amplitude (y_c^{stat}) are also shown. (b) Phase space trajectory (black) in wavy flow for initial conditions $(y_{c,0}, \psi_0) = (0.05d, 0)$, approaching the limit cycle (red).

transitions to swinging, and finally approaches the fixed point $(y_c, \psi) = (0, 0)$, corresponding to an upstream orientation of the swimmer at the channel center. Here, the flow vorticity is zero and hence the swimmer is not reoriented anymore. For wavy flow lines, the vorticity is nonzero everywhere in the channel and causes the swimmer to oscillate periodically about its mean upstream orientation, resulting in a swinging motion. Choosing $u_0 > v_0$, swimmers drift downstream for both planar and wavy flows. The short-time transient of the wavy-induced swinging motion depends on the swimmer's initial position and orientation, but the long-time behavior does not, as indicated by the red dashed and blue dotted trajectories in Fig. 3(a). In the following, we refer to the constant long-time swinging amplitude as y_c^{stat} and to the maximal oscillation amplitude during the transient regime as y_c^{max}, as indicated in Fig. 3(a). Figure 3(b) shows the phase space trajectory for a swimmer starting with an upstream orientation from a lateral position near the center of the wavy channel that converges to a periodic trajectory (limit cycle).

The dependence of the wavy-induced swinging motion of the microswimmer as a function of the channel's modulation length λ and amplitude ε will now be examined in more detail. We compute y_c^{stat} by the maximum of the magnitude of $y_c(t)$ beyond the transient regime in $t \in [1, 2] \times 10^6$. For small oscillations, the swinging frequency of an elongated microswimmer in planar Poiseuille flow is given by $\omega_0 = \sqrt{u_0 v_0 (1 - G)}/d$ [18], with geometry factor $G = (r_p^2 - 1)/(r_p^2 + 1)$ and swimmer aspect ratio $r_p = 1 + (N - 1)b/(2a)$. An additional frequency ω_{Ch} is imposed on the swimmer when it moves along wavy streamlines. Assuming a perfect upstream swimmer orientation yields $\omega_{\mathrm{Ch}} \approx 2\pi |u_0 - v_0|/\lambda$. In our system, ω_0 can be interpreted as the oscillator eigenfrequency and ω_{Ch} the frequency of an external periodic drive with amplitude ε. We expect the swinging amplitude to peak in the resonance case of $\omega_{\mathrm{Ch}} \approx \omega_0$, which determines a resonance wavelength via

$$\lambda_{\mathrm{res}} \approx \frac{2\pi d |u_0 - v_0|}{\sqrt{u_0 v_0 (1 - G)}}. \tag{4}$$
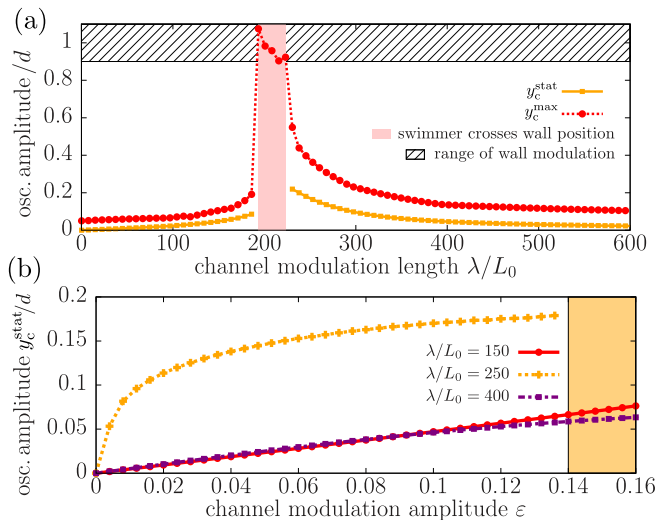
FIG. 4. (a) Resonance curve with steady-state (y_c^{stat}, orange bold line, squares) and maximum amplitude (y_c^{max}, red dotted line, circles) vs modulation length λ in units of the swimmer length L_0. The black shaded rectangle indicates the range of wall modulation ($\varepsilon = 0.1$). (b) y_c^{stat} vs modulation amplitude ε for $\lambda/L_0 = 150$ below (red bold lines, circles) and $\lambda/L_0 = 400$ beyond the resonance wavelength (violet dashed-dotted lines, squares). For $\lambda/L_0 = 250$ close to λ_{res} (orange dotted lines) the swimmer crosses the wall position in the orange range.

Figure 4(a) shows the swinging amplitude vs λ. For small wavelengths, both the initial and steady-state response of the system are small, with $y_c^{\text{stat}} \to 0$ for $\lambda \to 0$. This case corresponds to a very large ω_{Ch}. Increasing λ causes increasing maximum and steady-state oscillation amplitudes, culminating in a peak of y_c^{max} in the range of $193 \lesssim \lambda/L_0 \lesssim 223$ [light red area in Fig. 4(a)]. For this λ, the transient swimmer response is large enough that one of its beads reaches the wall position. In this case, we stop the simulation in unbounded flows. The influence of repulsive swimmer-wall interactions will be discussed in Sec. V. For further growing λ, y_c^{max} and y_c^{stat} decrease monotonically and approach a small but finite amplitude for large wavelengths. With the parameters listed in [40], we obtain $\lambda_{\text{res}} \approx 257 L_0$ from Eq. (4), which is close to the resonance region in Fig. 4(a). The difference between this theoretical prediction and the numerics arises from the assumption of perfect upstream orientation and a constant swimmer position at the channel center. For increasing swinging amplitudes, i.e., for $\lambda \approx \lambda_{\text{res}}$, the swimmer on average visits positions further away from the channel center more often where the flow is slower. Thus ω_{Ch} is effectively smaller than assumed above.

Increasing ε results in a growing size of the limit cycle, as shown in Fig. 4(b). That applies to λ smaller, larger, and close to the λ_{res} [cf. Fig. 4(a)]. In the latter case, we observe crossings of wall positions by the swimmer during the initial transient for $\varepsilon > 0.14$. For the effect of F_0 on the swimmer behavior in the wavy channel, see Appendix G.

Apart from the channel geometry, the experimentally controllable flow strength significantly impacts the swimmer behavior in the wavy channel. We choose $\lambda = 150 L_0$, a wave-
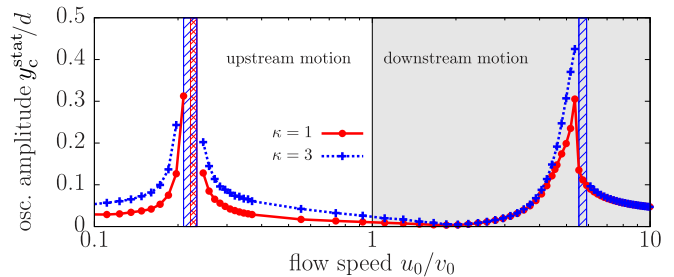

FIG. 5. Steady-state swinging amplitude y_c^{stat}/d vs velocity ratio u_0/v_0 is larger for stiffer swimmers ($\kappa = 3$, blue dotted lines, crosses) than for softer ones ($\kappa = 1$, red bold lines, circles), with upstream (white, left panel) and downstream resonance (gray, right panel). The swimmer exceeds the wall position in certain ranges of u_0/v_0 (blue dashed boxes for $\kappa = 3$ and red double-dashed box for $\kappa = 1$).

length smaller than λ_{res} in Fig. 4(a), and show in Fig. 5 the steady-state swinging amplitude vs the normalized flow amplitude for different rigidities $\kappa = 1, 3$. We observe resonant behavior for both upstream ($u_0 < v_0$) and downstream motion ($u_0 > v_0$). Depending on κ, the resonant oscillations can become large enough to trigger a crossing of one of the channel wall positions. Flow speed ranges above and below the respective resonance ratio u_0/v_0 are characterized by a comparably small y_c^{stat}. Assuming fixed λ, we solve Eq. (4) for u_0/v_0, yielding

$$\frac{u_0}{v_0} = 1 + \frac{\alpha^2}{2}(1 - G) \pm \alpha \sqrt{(1 - G) + \frac{\alpha^2}{4}(1 - G)^2}, \quad (5)$$

where $\alpha := \lambda/(2\pi d) > 0$ depends only on the channel's geometry. Equation (5) has the two solutions $u_0/v_0 = 4.54$ (downstream drift) and $u_0/v_0 = 0.22$ (upstream swimming). Both give a good approximation for the location of the numerically obtained maxima in Fig. 5. Our predictions for ω_0 and ω_{Ch} agree well with the numerically obtained Fourier spectra of the swimmer trajectory; see Appendix H.

V. EFFECTS OF CONFINEMENT

For increased vicinity of the swimmer to the channel walls, confinement effects become important. This is especially the case for large flow amplitudes compared to the swimmer's speed, where the repellers in plane channels are located close to the channel center and thus outward migration dominates. In order to account for wall effects in our simulations, we include a short-range repulsive potential at the channel boundaries [41], as described in Appendix I.

For a large ratio $u_0/v_0 = 107$ we find in plane channel repellers at $y \approx \pm d/4$. Swimmers located outside of the repellers migrate closer to the walls and then tumble around a constant y position, resulting in an attractor close to each of the walls [blue bold trajectory in Fig. 6(a)]. In wavy flows, tumbling has a significantly larger amplitude and a periodicity of 4λ [red dashed trajectory in Fig. 6(a)]. Figure 6(b) shows swimmer trajectories averaged over 4λ on a longer time scale. As described in Sec. III, outward CSM takes place in plane flows, whereas no lateral drift occurs in wavy channels where $\langle y_c \rangle$ is closer to the center for large times. In plane flows
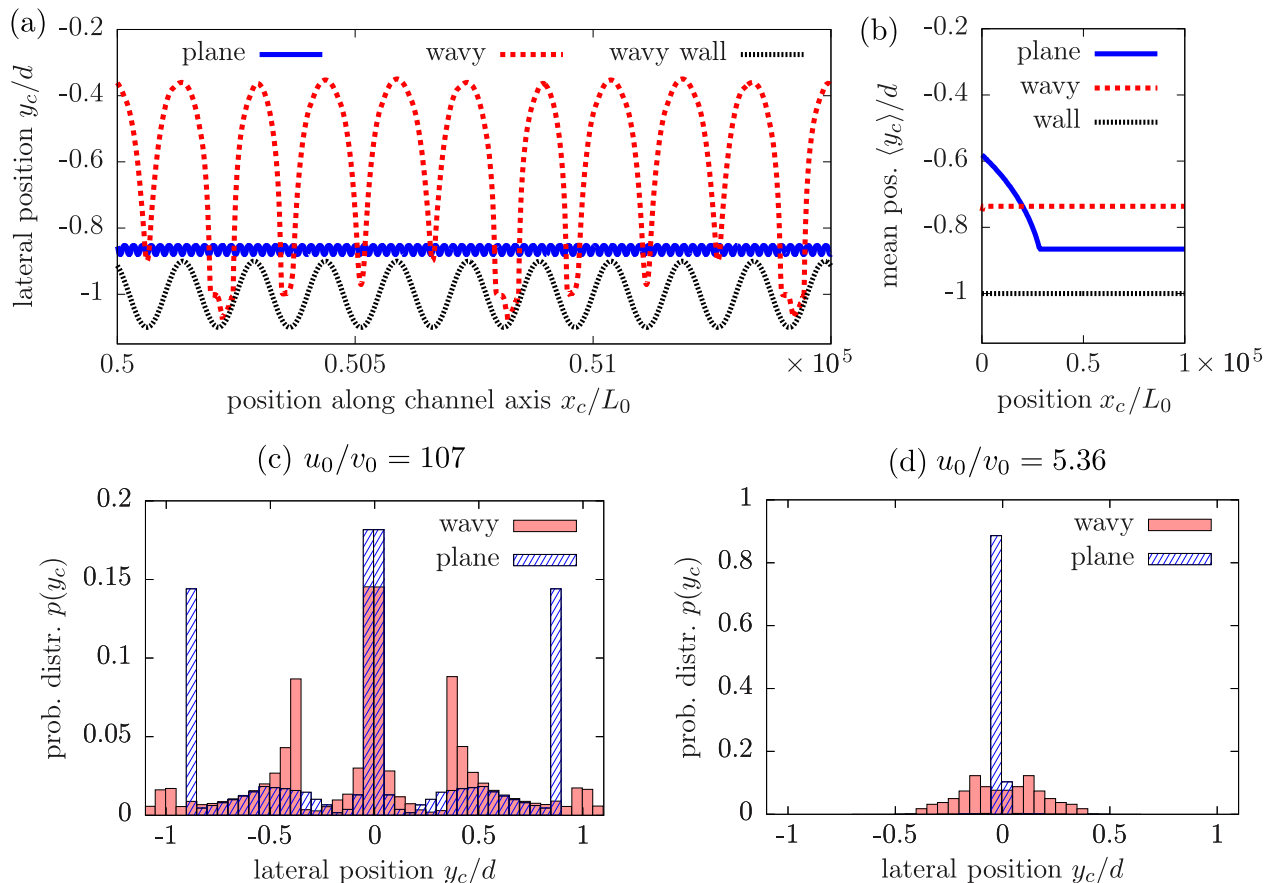
FIG. 6. (a) Individual and (b) mean trajectories for a swimmer starting at $y_{c,0} = -0.6d$ in straight (blue bold line) and wavy streamlines (red dashed line) with $u_0 = 107v_0$. Black dotted line is the wavy channel boundary in (a) and its mean at $y_w/d = -1$ in (b). The plane boundary is at $y_w/d = -1$ in both cases. (c) Probability distribution $p(y_c)$ of a swimmer in straight (dashed blue bars) and wavy streamlines (bold red bars) for $u_0/v_0 = 107$ and in (d) for $u_0/v_0 = 5.36$.

the swimmer migrates by a lateral distance of $0.32d$ while traveling $2.9 \times 10^4 L_0$ in x direction [blue bold trajectory in Fig. 6(b)]. By contrast, lateral motion in wavy flows is fast: the large tumbling amplitude enables the swimmer to move up to $0.71d$ in y direction while being advected downstream only $86L_0$.

Figures 6(c) and 6(d) show the lateral probability distribution $p(y_c)$ in the plane and wavy flow. We obtain $p(y_c)$ by averaging individual swimmer distributions for 10 different initial positions $y_{c,0} \in [-d/2, d/2]$. Each individual distribution is determined during the simulation time $t_{end} = 3 \times 10^7$. $p(y_c)$ is displayed for large u_0/v_0 and a 20 times smaller ratio, $u_0/v_0 = 5.36$, where wavy-induced swinging becomes resonant (cf. Fig. 5). The repellers cause swimmers in plane channels to accumulate for large u_0/v_0 either at the center or at an attractor close to each wall [three peaks in Fig. 6(c)]. The small probabilities between the peaks of $p(y_c)$ result from the transient CSM to the attractors. By contrast, the large amplitude of wavy-induced tumbling, as shown in Fig. 6(a), leads to small values of $p(y_c)$ near the walls, i.e., swimmer depletion at the walls. For smaller u_0/v_0, swimmers migrate to the center of plane channels for all initial positions, resulting in a single peak of $p(y_c)$ at $y_c = 0$ in Fig. 6(d). This behavior is changed in wavy flows where the wavy-induced swinging

motion broadens $p(y_c)$ and reduces the swimmer probability at the channel center significantly.

VI. CONCLUSION

In this work, we analyzed the behavior of elongated semi-flexible microswimmers, such as bacteria, in flows through both plane and wavy microchannels. In plane channels, swimmers migrate during tumbling across streamlines either towards the channel center or towards one of the walls. The migration direction depends on the swimmer's initial lateral position and the ratio of flow strength over the swimmer's speed. If this ratio is small, swimmers first migrate inwards and then reorient against the flow. In a suspension of swimmers, this can lead to accumulation at the channel center which may facilitate the formation of swimmer clusters [42]. For large ratios of flow strength over swimming speed, we find that swimmers migrate away from the channel center towards attractors close to the walls. This can, in addition to clustering, promote the formation of bacterial biofilms at the boundaries [43], as well as upstream migration due to surface rheotaxis [44,45]. In general, surface accumulation can have different origins and take place already for rigid swimmers [37]. The mechanism described here results from the lateral

migration of swimmers in the bulk, which is driven by their deformability.

We demonstrated that the wavy channel significantly alters the swimmer's behavior in both cases. For small ratios of flow strength over swimming speed, we report on a wavy-induced swinging motion that is independent of the swimmer's initial conditions and disturbs the convergence to the center line. The size of the associated limit cycle can be controlled by the flow velocity, the swimmer's speed and size, and the boundary modulation. We discovered a resonance effect where the swinging amplitude becomes large enough that swimmers cross the entire channel periodically and the probability distribution becomes broad. Near the resonance, bacteria are forced to hit the walls where they can be killed, e.g., by nanopillars [46] or antibacterial surface coatings [47]. Since the resonance is observed for both upstream and downstream motion of the swimmer, bacteria can be ejected from the channel center regardless of their swimming direction. In the case of large flow velocities compared to the swimming speed, we identify a wavy-induced tumbling motion. It is characterized by a much larger amplitude than the well-known tumbling of swimmers in plane Poiseuille flow. As a result, swimmers are depleted in regions close to the walls, aiding the suppression of surface rheotaxis.

We expect hydrodynamic swimmer-wall interactions [48] to affect our results quantitatively, but not fundamentally. Possible emergent behavior due to noise effects [49,50] and chirality of flagella [4] are the subject of future studies.

APPENDIX A: MOBILITY MATRICES, FORCES, AND TORQUES

The mobility matrix in Eq. (1a) mediates the hydrodynamic interaction for the translational degrees of freedom and is given by the Rotne-Prager tensor for differently sized beads [32]:

$$
\boldsymbol{\mu}_{ij}^{\mathrm{tt}} = \begin{cases} \frac{1}{8\pi\eta\tilde{r}}\left[\left(1+\frac{a_i^2+a_j^2}{3\tilde{r}^2}\right)\mathbf{1} + \left(1-\frac{a_i^2+a_j^2}{\tilde{r}^2}\right)\frac{\tilde{\mathbf{r}}\otimes\tilde{\mathbf{r}}}{\tilde{r}^2}\right] & \text{for}\quad \tilde{r} > a_i + a_j, \\ \frac{1}{6\pi\eta a_i a_j}\left[\frac{16\tilde{r}^3(a_i+a_j)-\left[(a_i-a_j)^2+3\tilde{r}^2\right]^2}{32\tilde{r}^3}\mathbf{1} + \frac{3\left[(a_i-a_j)^2-\tilde{r}^2\right]^2}{32\tilde{r}^3}\frac{\tilde{\mathbf{r}}\otimes\tilde{\mathbf{r}}}{\tilde{r}^2}\right] & \text{for}\quad a_i + a_j \geqslant \tilde{r} > a_> - a_<, \\ \frac{1}{6\pi\eta a_>}\mathbf{1} & \text{for}\quad \tilde{r} \leqslant a_> - a_<, \end{cases}
\tag{A1}
$$

with the bead-to-bead vector $\tilde{\mathbf{r}} := \mathbf{r}_i - \mathbf{r}_j$ and its modulus $\tilde{r} = |\tilde{\mathbf{r}}|$. The identity matrix is $\mathbf{1}$ and $\tilde{\mathbf{r}} \otimes \tilde{\mathbf{r}}$ denotes the outer product of $\tilde{\mathbf{r}}$ with itself. In the pair i, j, $a_>$ and $a_<$ are the bead radii of the larger or smaller bead, respectively. The counterforce point is treated as an additional bead with radius 0, located at $\mathbf{r}_\mathrm{p} = \mathbf{r}_N - 2a\hat{\mathbf{e}}_s$ and subjected only to the force $\mathbf{F}_\mathrm{p} = -\mathbf{F}_0$. The flow disturbance caused by $\mathbf{F}_\mathrm{p}$ accounts for the $N + 1$st contribution to the translational and angular velocities in the sums of Eqs. (1), with $\mathbf{F}_{N+1} = \mathbf{F}_\mathrm{p}$.

Together, the forces on each point of the swimmer are

$$
\mathbf{F}_i = \begin{cases} -\nabla_i(V_i^\mathrm{H} + V_i^\mathrm{B}) & \text{for}\quad i \in [1, N-1], \\ -\nabla_i(V_i^\mathrm{H} + V_i^\mathrm{B}) + \mathbf{F}_0 & \text{for}\quad i = N, \\ -\mathbf{F}_0 & \text{for}\quad i = N+1, \end{cases}
\tag{A2}
$$

with V_i^H and V_i^B for each bead as described above. The elastic (nonactive) bead forces compensate each other:

$$
\sum_{i=1}^{N} -\nabla_i\left(V_i^\mathrm{H} + V_i^\mathrm{B}\right) = \mathbf{0}.
\tag{A3}
$$

From Eq. (A2) then follows that the total swimmer, i.e., all N beads and the counterforce point, is force free:

$$
\sum_{i=1}^{N+1} \mathbf{F}_i = \mathbf{0}.
\tag{A4}
$$

We note that, by including only translational degrees of freedom in the equations of motion for each bead, the flow-vorticity-induced rotation of our swimmer in a shear flow with straight streamlines (e.g., a linear shear or plane Poiseuille flow) would come to a halt as soon as the zimmer axis is aligned with the flow direction. However, any object with a finite aspect ratio will perform a continuous rotation under shear flow, known as Jeffery orbits [51]. For this reason, we include also rotational degrees

of freedom in our model. The corresponding mobility matrices are given by [32]

$$
\boldsymbol{\mu}_{ij}^{\mathrm{rr}} = \begin{cases} -\frac{1}{16\pi\eta\tilde{r}^3}\left(\mathbf{1} - 3\frac{\tilde{\mathbf{r}}\otimes\tilde{\mathbf{r}}}{\tilde{r}^2}\right) & \text{for} \quad \tilde{r} > a_i + a_j, \\ \frac{1}{8\pi\eta a_i^3 a_j^3}\left(\alpha\mathbf{1} + \beta\frac{\tilde{\mathbf{r}}\otimes\tilde{\mathbf{r}}}{\tilde{r}^2}\right) & \text{for} \quad a_i + a_j \geqslant \tilde{r} > a_> - a_<, \\ \frac{1}{8\pi\eta a_>^3}\mathbf{1} & \text{for} \quad \tilde{r} \leqslant a_> - a_<, \end{cases}
\tag{A5}
$$

with coefficients

$$
\alpha = \frac{5\tilde{r}^6 - 27\tilde{r}^4(a_i^2 + a_j^2) + 32\tilde{r}^3(a_i^3 + a_j^3) - 9\tilde{r}^2(a_i^2 - a_j^2)^2 - (a_i - a_j)^4(a_i^2 + 4a_i a_j + a_j^2)}{64\tilde{r}^3},
$$

$$
\beta = \frac{3[(a_i - a_j)^2 - \tilde{r}^2]^2(a_i^2 + 4a_i a_j + a_j^2 - \tilde{r}^2)}{64\tilde{r}^3},
\tag{A6}
$$

as well as

$$
\boldsymbol{\mu}_{ij}^{\mathrm{rt}} = \begin{cases} \frac{1}{8\pi\eta\tilde{r}^2}\varepsilon\frac{\tilde{\mathbf{r}}}{\tilde{r}} & \text{for} \quad \tilde{r} > a_i + a_j, \\ \frac{1}{16\pi\eta a_i^3 a_j}\frac{(a_i - a_j + \tilde{r})^2[a_j^2 + 2a_j(a_i + \tilde{r}) - 3(a_i - \tilde{r})^2]}{8\tilde{r}^2}\varepsilon\frac{\tilde{\mathbf{r}}}{\tilde{r}} & \text{for} \quad a_i + a_j \geqslant \tilde{r} > a_> - a_<, \\ \theta(a_i - a_j)\frac{\tilde{r}}{8\pi\eta a_i^3}\varepsilon\frac{\tilde{\mathbf{r}}}{\tilde{r}} & \text{for} \quad \tilde{r} \leqslant a_> - a_<, \end{cases}
\tag{A7}
$$

with $(\varepsilon\tilde{\mathbf{r}})_{\alpha\beta} = \varepsilon_{\alpha\beta\gamma}\tilde{r}_\gamma$ and the Heaviside function $\theta(x)$. $\boldsymbol{\mu}_{ij}^{\mathrm{tr}}$ is obtained by interchanging beads i and j in Eq. (A7). We furthermore introduce two vectors $\mathbf{p}_i$ and $\mathbf{q}_i$ for each bead, characterizing its instantaneous orientation. We control the otherwise free rotation of the beads by the bead torque

$$
\mathbf{T}_i = \frac{\kappa_\mathrm{t}}{2}\left[\mathbf{p}_i \times \left(\hat{\mathbf{e}}_i^\parallel + \hat{\mathbf{e}}_{i-1}^\parallel\right) + \mathbf{q}_i \times \left(\hat{\mathbf{e}}_i^\perp + \hat{\mathbf{e}}_{i-1}^\perp\right)\right].
\tag{A8}
$$

Here, κ_t is the torque strength and $\hat{\mathbf{e}}_i^\parallel$ the unit vector pointing from bead i in the direction of the next bead in the chain. $\hat{\mathbf{e}}_i^\perp$ is the unit vector perpendicular to $\hat{\mathbf{e}}_i^\parallel$, which is obtained by shifting the polar angle of $\hat{\mathbf{e}}_i^\parallel$ in spherical coordinates by $\pi/2$ (cf. Fig. 7). The orientation of each bead is then evolved via

$$
\dot{\mathbf{p}}_i = \boldsymbol{\Omega}_i \times \mathbf{p}_i, \quad \dot{\mathbf{q}}_i = \boldsymbol{\Omega}_i \times \mathbf{q}_i.
\tag{A9}
$$

In the case of a straight (undeformed) chain, the torque for bead i according to Eq. (A8) is minimal when $\mathbf{p}_i$ points towards its neighboring bead to the right and $\mathbf{q}_i$ in the direction of $\hat{\mathbf{e}}_i^\perp$. Deviations of $\mathbf{p}_i$ or $\mathbf{q}_i$ from this configuration are penalized with a restoring torque $\mathbf{T}_i$. This torque then couples to the translational and angular velocities of all beads of the chain via Eqs. (1). As a result, rotations of individual beads translate to a rotation of the entire chain. As we show below,
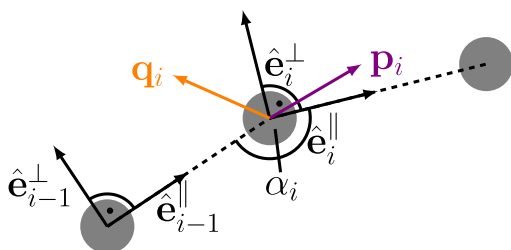
by this we reproduce Jeffery orbits of a stiff passive chain in a shear flow.

APPENDIX B: JEFFERY DYNAMICS OF A PASSIVE ROD IN LINEAR SHEAR FLOW

In a linear shear flow, the period for a rigid rod with aspect ratio r_p to perform one Jeffery orbit has been derived as [52]

$$
T = \frac{2\pi}{\dot{\gamma}}\left(r_\mathrm{p} + \frac{1}{r_\mathrm{p}}\right),
\tag{B1}
$$

which is also referred to as the tumbling time. We use Eq. (B1) to fit our parameters in order to obtain a realistic behavior of our model. For this we focus on a passive chain of beads ($F_0 = 0$) with negligible deformability ($k = \kappa = 100$) in linear shear flow $\mathbf{u}(\mathbf{r}_i) = \dot{\gamma}y_i\hat{\mathbf{e}}_x$ with shear rate $\dot{\gamma} = 0.1$. We keep $a = 0.5$ constant and vary b in order to adapt the aspect ratio $r_\mathrm{p} = 1 + (N - 1)b/(2a)$. Figure 8 shows the simulation results for three rods with different numbers of beads N together with the theoretical prediction of Eq. (B1). For small aspect ratios, the tumbling time of the rod lies below the theoretical

FIG. 7. Segment of the chain around bead i with opening angle α_i. The torque according to Eq. (A8) penalizes deviations of the orientation vectors $\mathbf{p}_i$ (violet) and $\mathbf{q}_i$ (orange) from the local unit vectors along and perpendicular to the axis connecting neighboring beads (black dashed line)
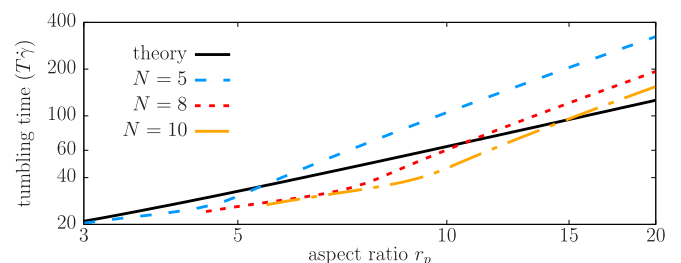
FIG. 8. Tumbling time T of a passive, stiff chain of beads in a linear shear flow with the shear rate $\dot{\gamma}$ as a function of the aspect ratio r_p for different numbers of beads N. Blue dashed lines correspond to $N = 5$, red dashed lines to $N = 8$, and orange dashed lines to $N = 10$. The black bold line shows the theoretical prediction according to Eq. (B1). Larger values of N match the prediction when higher aspect ratios are chosen (intersections with the black line).
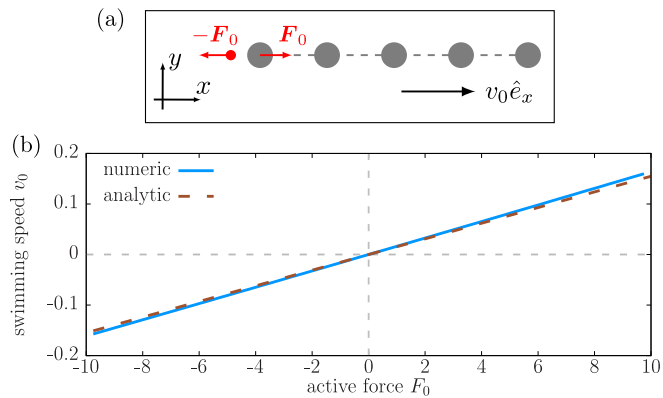
FIG. 9. (a) Sketch of a swimmer with $N = 5$ beads in a linear configuration. The force dipole (red arrows) is located at its left and the resulting swimming velocity $v_0\hat{e}_x$ is directed along the x axis. (b) Calibration curve for the intrinsic swimming speed v_0 (propulsion speed without incident flow) as a function of the active force's absolute value F_0 for the stiff swimmer. The results of the analytical calculation (brown dashed line) according to Eq. (C2) and the numerical simulation (blue bold line) are shown.

prediction. T then grows as function of r_p. We find that, for each number of beads, the numerically determined values for T match with Eq. (B1) for one aspect ratio. In this work, we limit our studies to $N = 5$, where we find optimal agreement for an aspect ratio of 5.38, corresponding to $b = 1.095$. These parameters are used for all of our simulations.

APPENDIX C: INTRINSIC SWIMMING SPEED

In our swimmer model, self-propulsion is achieved by the active force $\mathbf{F}_0$ at the swimmer's rear end. The relevant physical quantity, however, is the resulting intrinsic swimming speed v_0. In a quiescent fluid ($u_0 = 0$) we approximate v_0 as function of F_0 analytically for a nondeformable swimmer. For this, we neglect bead rotations as well as the hydrodynamic

flow field created by the elastic forces and take into account only the flow field originating from the pair of active forces. We consider a swimmer initially aligned with the x axis with beads positioned at $\mathbf{r}_i = [-(i-1)b, 0, 0]$ with $i = 1, \ldots, N$, and the counterforce point located at $\mathbf{r}_p = [-(N-1)b - 2a, 0, 0]$ [cf. Fig. 9(a)].

We consider a stiff swimmer, so the motion of the beads relative to each other can be neglected. With Eqs. (1), the simplified equations of motion for the swimmer velocity then yield

$$\dot{\mathbf{r}}_c = \frac{1}{N}\sum_{i=1}^{N}\dot{\mathbf{r}}_i = \frac{1}{N}\sum_{i=1}^{N}\left(\frac{\mathbf{F}_i}{6\pi\eta a} + \sum_{j=1, j\neq i}^{N}\boldsymbol{\mu}_{ij}^{tt}\cdot\mathbf{F}_j + \boldsymbol{\mu}_{ip}^{tt}\cdot\mathbf{F}_p\right),$$

(C1)

where $\boldsymbol{\mu}_{ip}^{tt}$ describes the hydrodynamic interaction between bead i and the counterforce point, according to Eq. (A1). Using $\mathbf{F}_N = F_0\hat{\mathbf{e}}_x$, $\mathbf{F}_p = -F_0\hat{\mathbf{e}}_x$, and $\mathbf{F}_i = \mathbf{0}$ for $i = 1, \ldots, N-1$, it follows from Eq. (A1) $\dot{\mathbf{r}}_c = v_0\hat{\mathbf{e}}_x$ with

$$v_0 = \frac{F_0}{4\pi\eta N}\left\{\frac{5}{24a} + \sum_{i=1}^{N-1}\frac{1}{(N-i)b}\left[1 - \frac{2a^2}{3(N-i)^2b^2}\right]\right.$$
$$\left. - \frac{1}{[(N-i)b + 2a]}\left[1 - \frac{a^2}{3[(N-i)b + 2a]^2}\right]\right\}. \quad (C2)$$

Equation (C2) is the velocity due to the Stokes friction of the Nth bead, together with the contributions of the flow field created by the force dipole on all beads of the chain. This result is shown in Fig. 9(b) for $N = 5$ together with the numerically obtained values for the intrinsic swimming speed. In the simulation we choose $k = \kappa = 100$ to ensure negligible deformation. For $F_0 > 0$ a pusher-type flow field is created by the two opposite active forces and the swimmer moves in positive x direction, whereas for $F_0 < 0$ we obtain a puller-type flow field and motion in negative x direction. Differences between the analytical and numerical results arise from the approximation of zero bead forces, but overall good agreement is observed. We use the numerically obtained values for v_0 as a function of F_0 in our analysis.

APPENDIX D: VALIDATION OF THE FAR FIELD AROUND THE SWIMMER

In the following we show that, as a direct consequence of the total force-free condition (A4) for our autonomous swimmer, the far field has a dipolar character; that is, it decays as the inverse squared distance from the swimmer. For this, we take into account a nonlinear configuration of the beads with numerical values as bead positions. We consider a swimmer which is deformed by a plane Poiseuille flow during tumbling. The numerically obtained bead positions are

$$\mathbf{r}_1 = \begin{pmatrix} 263.8 \\ 10.53 \\ 0 \end{pmatrix}, \quad \mathbf{r}_2 = \begin{pmatrix} 264.7 \\ 9.933 \\ 0 \end{pmatrix}, \quad \mathbf{r}_3 = \begin{pmatrix} 265.6 \\ 9.274 \\ 0 \end{pmatrix}, \quad \mathbf{r}_4 = \begin{pmatrix} 266.3 \\ 8.481 \\ 0 \end{pmatrix}, \quad \mathbf{r}_5 = \begin{pmatrix} 266.9 \\ 7.532 \\ 0 \end{pmatrix}, \quad \mathbf{r}_p = \begin{pmatrix} 267.4 \\ 6.663 \\ 0 \end{pmatrix}. \quad (D1)$$

See sketch in Fig. 10(a). The corresponding bead forces are

$$\mathbf{F}_1 = \begin{pmatrix} 2.292 \times 10^{-2} \\ -5.089 \times 10^{-3} \\ 0 \end{pmatrix}, \quad \mathbf{F}_2 = \begin{pmatrix} -1.488 \times 10^{-2} \\ 1.313 \times 10^{-2} \\ 0 \end{pmatrix}, \quad \mathbf{F}_3 = \begin{pmatrix} -4.182 \times 10^{-2} \\ 3.942 \times 10^{-2} \\ 0 \end{pmatrix}, \quad \mathbf{F}_4 = \begin{pmatrix} -4.841 \times 10^{-3} \\ -3.501 \times 10^{-2} \\ 0 \end{pmatrix},$$

$$\mathbf{F}_5 = \begin{pmatrix} -2.579 \times 10^{-1} \\ 5.092 \times 10^{-1} \\ 0 \end{pmatrix}, \quad \mathbf{F}_p = \begin{pmatrix} 2.965 \times 10^{-1} \\ -5.216 \times 10^{-1} \\ 0 \end{pmatrix}. \quad (D2)$$
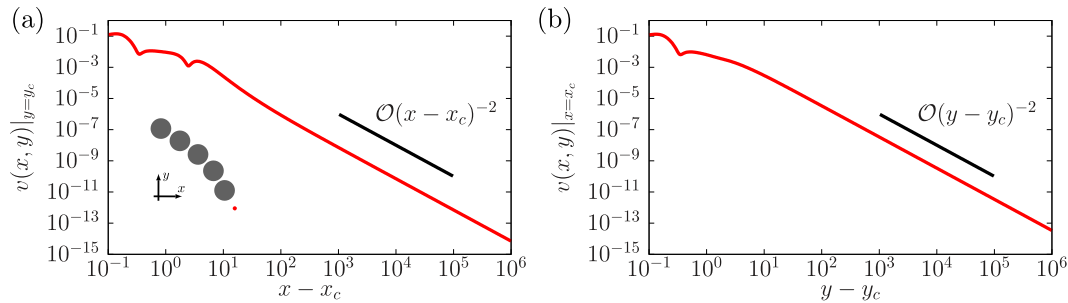
FIG. 10. Absolute value of the flow field $\mathbf{v}(\mathbf{r})$ according to Eq. (D3) (red line) for large distances from the swimmer's center $\mathbf{r}_c = (x_c, y_c, z_c)$. The flow field decays as the inverse squared distance from the swimmer (see black line) in x direction (a), as well as in y direction (b). Inset in (a) shows numerically obtained bead positions according to Eq. (D1), with beads sketched in gray and the counterforce point in red.

We note that, in contrast to Appendix C, the full forces on each bead are taken into account here, including forces from bending and stretching of the chain. For simplicity, we only consider contributions to the flow field originating from the translational-translational mobility matrix. The flow field is then given by

$$\mathbf{v}(\mathbf{r}) = \sum_{j=1}^{N+1} \boldsymbol{\mu}_j^{tt}(\boldsymbol{\varrho}) \cdot \mathbf{F}_j, \quad \text{with } \boldsymbol{\mu}_j^{tt}(\boldsymbol{\varrho}) = \frac{1}{8\pi\eta\varrho}\left[\left(1 + \frac{a_j^2}{3\varrho^2}\right)\mathbf{1} + \left(1 - \frac{a_j^2}{\varrho^2}\right)\frac{\boldsymbol{\varrho}\otimes\boldsymbol{\varrho}}{\varrho^2}\right], \tag{D3}$$

with $\boldsymbol{\varrho} := \mathbf{r} - \mathbf{r}_j$ and $\varrho = |\boldsymbol{\varrho}|$. The absolute value of $\mathbf{v}(\mathbf{r})$ as function of the distance from the swimmer in x and y direction is shown in Figs. 10(a) and 10(b), respectively. For large distances, the flow field decays as the inverse squared distance. In particular, Stokeslets are nonexistent in the flow field since they would decay slower, namely as the inverse distance.

APPENDIX E: SWIMMER BEHAVIOR IN PLANE POISEUILLE FLOW

We further validate our model for the swimmer by analyzing its behavior in a plane Poiseuille flow. For this we employ stiff ($\kappa = 100$) and flexible swimmers ($\kappa = 0.5$) with an activity of $F_0 = 0.3$, resulting in an intrinsic swimming speed of $v_0 = 4.872 \times 10^{-3}$. Figure 11(a) shows the trajectory of a stiff swimmer (blue line) with negligible deformation in the flow. As reported previously [17,18], such a swimmer either performs a swinging motion or tumbles around a constant off-centered position in the channel that depends on its initial conditions. The corresponding periodic phase-space orbit is shown in Fig. 11(b). For an elongated swimmer, the angular velocity becomes a function of the instantaneous orientation angle [18]

$$\dot{\psi} = \frac{u_0}{d^2}y[1 - G\cos(2\psi)]. \tag{E1}$$

For a stiff swimmer we find very good agreement with Eq. (E1), as Fig. 11(c) shows. By contrast, a flexible swimmer [real space trajectory in Fig. 11(a), phase space trajectory in Fig. 11(b), red lines] in addition to its tumbling motion shows a lateral drift towards the channel center, enabling a tumbling swimmer to switch to swinging. This transition occurs below a critical y position when the flow vorticity $\nabla \times \mathbf{u} = 2u_0 y/d^2 \hat{\mathbf{e}}_z$ is not strong enough anymore to reorient the swimmer before it crosses the center [at $x/L_0 \approx 1.39 \times 10^3$ in Fig. 11(a)]. The amplitude of the swinging motion subsequently decreases and the swimmer approaches an attractor of upstream swimming at the centerline [$(y_c, \psi) = (0, 0)$]. This behavior has been found previously for microswimmers with flexible flagella [23,24].

APPENDIX F: ANALYTICAL DERIVATION OF THE FLOW FIELD IN THE WAVY CHANNEL

Here we derive analytically the solution for the flow field through serpentine wavy channels. The calculations are similar to the considerations in Refs. [39,53,54]. We have to solve

$$\nabla^4 \Psi(x, y) = 0, \tag{F1}$$

where $\Psi(x, y)$ is the stream function and $\nabla^4 = (\partial_x^2 + \partial_y^2)^2$ the biharmonic operator. The stream function fulfills the conditions

$$u_x(x, y) = \partial_y\Psi(x, y), \quad u_y(x, y) = -\partial_x\Psi(x, y). \tag{F2}$$

The walls of the wavy channel are at

$$y_{\mathrm{w}}(x) = d\left[\pm 1 + \varepsilon\,\sin\left(\frac{2\pi x}{\lambda}\right)\right]. \tag{F3}$$

One has the no-slip boundary conditions

$$u_x[x, y = y_{\mathrm{w}}(x)] = 0, \quad u_y[x, y = y_{\mathrm{w}}(x)] = 0. \tag{F4}$$

Furthermore, we assume point symmetry of the flow field around the origin of coordinates which is given by

$$u_{x,y}(-x, -y) = u_{x,y}(x, y). \tag{F5}$$

We start by introducing the dimensionless coordinates

$$x' := \frac{x}{\lambda}, \quad y' := \frac{y}{d}, \quad \Psi' := \frac{\Psi}{u_0 d}, \tag{F6}$$

where u_0 is the characteristic flow speed. With this, the plane coordinates

$$\eta(x') := x',$$
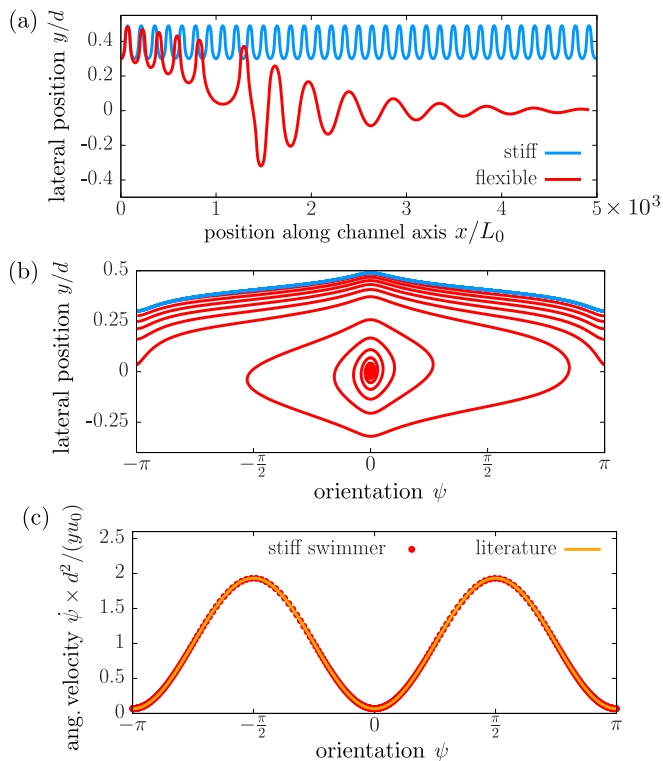$$\zeta(x', y') := y' - \varepsilon\,\sin\left(2\pi x'\right) \tag{F7}$$

FIG. 11. (a) Real space and (b) corresponding phase space trajectory of a flexible (red line) and a stiff swimmer (blue line) in plane Poiseuille flow with initial position $y_{c,0} = 0.3d$ and orientation $\psi_0 = \pm\pi$ (downstream). L_0 is the initial swimmer length and d is the channel half width. A stiff swimmer performs a tumbling motion around a fixed off-centered position (periodic phase space orbits). A flexible swimmer tumbles and simultaneously migrates towards the channel center, eventually switching to a swinging motion with decaying amplitude (see also Figs. 2 and 3). (c) Angular velocity $\dot{\psi}$ of a stiff swimmer (red dashed line) vs its instantaneous orientation ψ. The result agrees well with the theoretical prediction from the literature [Eq. (E1), orange bold line].

can be introduced where the walls are located at $\zeta = \pm 1$. The boundary conditions according to Eq. (F4) then transform into

$$\partial_\eta \Psi(\eta, \zeta)|_{\zeta=\pm 1} = 0, \qquad \partial_\zeta \Psi(\eta, \zeta)|_{\zeta=\pm 1} = 0, \tag{F8}$$

where $\Psi(\eta, \zeta)$ is the stream function in the plane coordinates that we have to calculate. For this, we translate the point symmetry according to Eq. (F5) into the new coordinates which yields

$$\partial_\zeta \Psi(-\eta, -\zeta) = \partial_\zeta \Psi(\eta, \zeta),$$
$$-\partial_\eta \Psi(-\eta, -\zeta) = -\partial_\eta \Psi(\eta, \zeta). \tag{F9}$$

This implies that $\Psi(\eta, \zeta)$ is an odd function of its arguments, namely $-\Psi(\eta, \zeta) = \Psi(-\eta, -\zeta)$. Equation (F1) then transforms into

$$\bar{\Delta}\bar{\Delta}\Psi(\eta, \zeta) = 0, \tag{F10}$$

where $\bar{\Delta}$ is the Laplace operator in the plane coordinates. Since ε is assumed to be small, a perturbation analysis is possible and thus the solution of Eq. (F10) can be written as

$$\Psi \approx \Psi_0 + \varepsilon\Psi_1, \tag{F11}$$

where Ψ_0 and Ψ_1 have to obey the boundary conditions (F8) separately. Substituting Eq. (F11) into Eq. (F10) and sorting the resulting terms with respect to orders in ε yields the equation for the zeroth order,

$$\partial_\zeta^4 \Psi_0(\zeta) = 0, \tag{F12}$$

which has the solution

$$\Psi_0(\zeta) = \zeta - \frac{\zeta^3}{3}. \tag{F13}$$

This can be substituted into the equation for the first order in ε, resulting in

$$\partial_\zeta^4 \Psi_1(\eta, \zeta) + 2\partial_\zeta^2\partial_\eta^2 \Psi_1(\eta, \zeta) + \partial_\eta^4 \Psi_1(\eta, \zeta) + \left[(16\zeta^2 - 16)\pi^4 - 16\pi^2\right]\sin(2\pi\eta) = 0. \tag{F14}$$

The solution of Eq. (F14) which is obtained by separation of variables is

$$\Psi_1(\eta, \zeta) = \frac{\sin(2\pi\eta)}{4\pi + \sinh(4\pi)}\left[-4\sinh(2\pi)\cosh(2\pi\zeta) + 4\zeta\ \sinh(2\pi\zeta)\cosh(2\pi) - 4(\zeta^2 - 1)\left(\frac{1}{2}\cosh(2\pi)\sinh(2\pi) + \pi\right)\right] \tag{F15}$$

and thus the total solution for the stream function up to $\mathcal{O}(\varepsilon^1)$ is

$$\Psi(\eta, \zeta) = \zeta - \frac{\zeta^3}{3} + \varepsilon\frac{4\sin(2\pi\eta)}{4\pi + \sinh(4\pi)}\left[-\sinh(2\pi)\cosh(2\pi\zeta) + \zeta\ \sinh(2\pi\zeta)\cosh(2\pi)\right.$$
$$\left.-(\zeta^2 - 1)\left(\frac{1}{2}\cosh(2\pi)\sinh(2\pi) + \pi\right)\right]. \tag{F16}$$

The expressions for the flow field in the physical coordinates can be calculated from Eq. (F16) according to

$$u_x'(x', y') = \partial_\eta \Psi(\eta, \zeta)\frac{d}{dy'}\eta(x', y') + \partial_\zeta \Psi(\eta, \zeta)\frac{d}{dy'}\zeta(x', y'), \tag{F17a}$$

$$u_y'(x', y') = -\partial_\eta \Psi(\eta, \zeta)\frac{d}{dx'}\eta(x', y') - \partial_\zeta \Psi(\eta, \zeta)\frac{d}{dx'}\zeta(x', y'). \tag{F17b}$$

By this we obtain solutions for $u'_x(x', y')$ and $u'_y(x', y')$, which are expanded again in powers of ε. The final expressions for the flow field are

$$u_x(x, y) = u_0 \left(1 - \frac{y^2}{d^2} + \varepsilon \frac{\sin(\frac{2\pi x}{\lambda})}{4\pi + \sinh(4\pi)} \left\{ [-8\pi \sinh(2\pi) + 4 \cosh(2\pi)] \sinh\left(\frac{2\pi y}{d}\right) \right. \right.$$

$$\left. \left. + \left[8\pi \cosh(2\pi)\cosh\left(\frac{2\pi y}{d}\right) - 4 \cosh(2\pi)\sinh(2\pi) + 2 \sinh(4\pi) \right] \frac{y}{d} \right\} \right), \tag{F18a}$$

$$u_y(x, y) = -u_0\, \varepsilon \cos\left(\frac{2\pi x}{\lambda}\right) \frac{2\pi}{4\pi + \sinh(4\pi)} \left[4 \cosh(2\pi)\frac{y}{d} \sinh\left(\frac{2\pi y}{d}\right) \right.$$

$$\left. - 4 \sinh(2\pi)\cosh\left(\frac{2\pi y}{d}\right) + [\sinh(4\pi) - 2 \cosh(2\pi)\sinh(2\pi)]\frac{y^2}{d^2} \right]. \tag{F18b}$$

With the functions

$$U_1(x, y) := \frac{\sin(\frac{2\pi x}{\lambda})}{4\pi + \sinh(4\pi)} \left\{ [-8\pi \sinh(2\pi) + 4 \cosh(2\pi)] \sinh\left(\frac{2\pi y}{d}\right) \right.$$

$$\left. + \left[8\pi \cosh(2\pi)\cosh\left(\frac{2\pi y}{d}\right) - 4 \cosh(2\pi)\sinh(2\pi) + 2 \sinh(4\pi) \right] \frac{y}{d} \right\}, \tag{F19a}$$

$$U_2(x, y) := -\cos\left(\frac{2\pi x}{\lambda}\right) \frac{2\pi}{4\pi + \sinh(4\pi)} \left[4 \cosh(2\pi)\frac{y}{d} \sinh\left(\frac{2\pi y}{d}\right) \right.$$

$$\left. - 4 \sinh(2\pi)\cosh\left(\frac{2\pi y}{d}\right) + [\sinh(4\pi) - 2 \cosh(2\pi)\sinh(2\pi)]\frac{y^2}{d^2} \right], \tag{F19b}$$

the flow field can be written as in Eqs. (3). In the special case of no wall modulation ($\varepsilon = 0$), we recover the plane Poiseuille flow profile

$$u_x = u_0 \left(1 - \frac{y^2}{d^2} \right), \tag{F20a}$$

$$u_y = 0 \tag{F20b}$$

from Eqs. (F18).

APPENDIX G: INFLUENCE OF SWIMMER ACTIVITY ON THE RESONANCE CURVE

Figure 12 shows three resonance curves for different swimmer activities. Generally, smaller activities result in larger
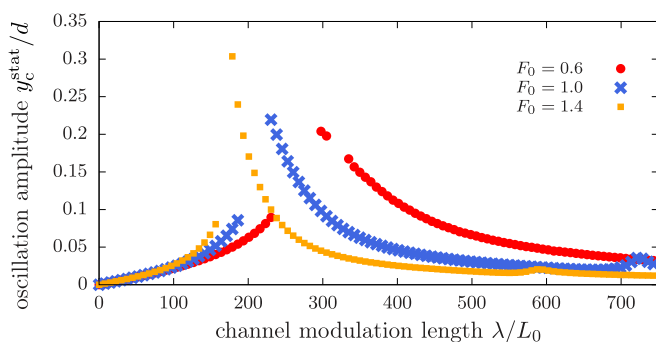
FIG. 12. Long-time oscillation amplitude y_c^{stat} in units of the channel half width d as function of the channel modulation length λ in units of the swimmer's initial length L_0. The results for three different activities $F_0 = 0.6$ (red circles), $F_0 = 1.0$ (blue crosses), and $F_0 = 1.4$ (orange squares) are shown.

oscillation amplitudes. Furthermore, we observe a shift of the maximum towards larger values of λ for decreasing F_0. This is in accordance with Eq. (4), which predicts the resonance wavelength to decrease as function of v_0 in the regime of downstream drift.

APPENDIX H: FOURIER SPECTRA OF THE SWIMMER TRAJECTORY

We calculate the Fourier spectrum of the swimmer's lateral position, $y_c(t)$. Figure 13(a) shows the spectrum for a swimmer with $\kappa = 3$ for $u_0/v_0 = 0.554$, which leads to an off-resonant oscillation with small amplitude (cf. Fig. 5). We observe two maxima in the spectrum that are close to the theoretical approximations for ω_0 and ω_{Ch}, as described above. For a flow strength close to the resonance case [$u_0/v_0 = 0.197$; cf.
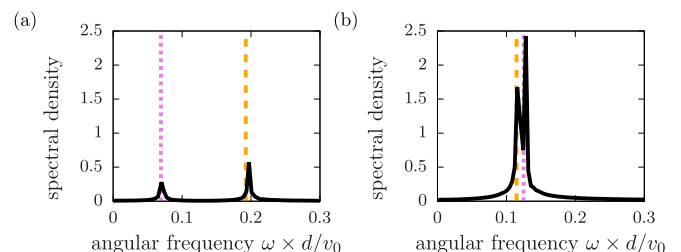
FIG. 13. Spectra $P(\omega)$ of the swimmer's lateral position as function of time, $y_c(t)$, for $u_0/v_0 = 0.554$ [(a), off resonant] and $u_0/v_0 = 0.197$ [(b), close to resonance], and the predictions for ω_0 (orange dashed lines) and ω_{Ch} (pink dotted lines).

Fig. [13(b)], both the theoretical and numerical locations for the maxima are shifted closer to each other.

APPENDIX I: REPULSIVE WALL POTENTIAL

To prevent the swimmer from crossing the position of the channel walls we include a short-range repulsive potential [41]

$$V(r_i^{\mathrm{w}}) = \begin{cases} V^*(r_i^{\mathrm{w}}) & \text{for} \quad r_i^{\mathrm{w}} \leqslant r^{\mathrm{w,c}}, \\ 0 & \text{for} \quad r_i^{\mathrm{w}} > r^{\mathrm{w,c}}, \end{cases} \quad \text{(I1)}$$

with

$$V^*(r_i^{\mathrm{w}}) = 4V_0\left[\left(\frac{\sigma}{r_i^{\mathrm{w}}}\right)^{12} - \left(\frac{\sigma}{r_i^{\mathrm{w}}}\right)^{6}\right]. \quad \text{(I2)}$$

Here r_i^{w} is the shortest distance between position of bead i to the wavy channel wall, $V_0 = 0.05$ is the repulsion energy, and $\sigma = 2^{-\frac{1}{6}}a$ is the repulsion length. The cutoff distance $r^{\mathrm{w,c}} = 2^{\frac{1}{6}}\sigma$ is chosen in such a way that only the repulsive part of Eq. [(I2)] is taken into account.

[1] R. Rusconi, J. S. Guasto, and R. Stocker, Bacterial transport suppressed by fluid shear, Nat. Phys. **10**, 212 (2014).

[2] G. L. Miño, M. D. Baabour, R. H. Chertcoff, G. O. Gutkind, E. Clément, H. Auradou, and I. P. Ippolito, E coli accumulation behind an obstacle, Adv. Microbiol. **08**, 451 (2018).

[3] G. Junot, N. Figueroa-Morales, T. Darnige, A. Lindner, R. Soto, H. Auradou, and E. Clément, Swimming bacteria in Poiseuille flow: The quest for active Bretherton-Jeffery trajectories, Europhys. Lett. **126**, 44003 (2019).

[4] A. J. T. M. Mathijssen, N. Figueroa-Morales, G. Junot, E. Clément, A. Lindner, and A. Zöttl, Oscillatory surface rheotaxis of swimming *E. coli* bacteria, Nat. Commun. **10**, 3434 (2019).

[5] N. Figueroa-Morales, A. Rivera, R. Soto, A. Lindner, E. Altshuler, and E. Clément, *E. coli* "super-contaminates" narrow ducts fostered by broad run-time distribution, Sci. Adv. **6**, eaay0155 (2020).

[6] F. P. Bretherton and N. M. V. Rothschild, Rheotaxis of spermatozoa, Proc. Royal Soc. London B **153**, 490 (1961).

[7] K. Miki and D. E. Clapham, Rheotaxis guides mammalian sperm, Curr. Biol. **23**, 443 (2013).

[8] V. Kantsler, J. Dunkel, M. Blayney, and R. E. Goldstein, Rheotaxis facilitates upstream navigation of mammalian sperm cells, eLIFE **3**, e02403 (2014).

[9] A. Bukatin, I. Kukhtevich, N. Stoop, J. Dunkel, and V. Kantsler, Bimodal rheotactic behavior reflects flagellar beat asymmetry in human sperm cells, Proc. Natl. Acad. Sci. U.S.A. **112**, 15904 (2015).

[10] N. Waisbord, A. Dehkharghani, and J. S. Guasto, Fluidic bacterial diodes rectify magnetotactic cell motility in porous environments, Nat. Commun. **12**, 5949 (2021).

[11] J. Palacci, S. Sacanna, A. Abramian, J. Barral, K. Hanson, A. Y. Grosberg, D. J. Pine, and P. M. Chaikin, Artificial rheotaxis, Sci. Adv. **1**, e140021 (2015).

[12] L. Ren, D. Zhou, Z. Mao, P. Xu, T. J. Huang, and T. E. Mallouk, Rheotaxis of bimetallic micromotors driven by chemical–acoustic hybrid power, ACS Nano **11**, 10591 (2017).

[13] W. Uspal, M. N. Popescu, S. Dietrich, and M. Tasinkevych, Rheotaxis of spherical active particles near a planar wall, Soft Matter **11**, 6613 (2015).

[14] Q. Brosseau, F. Balboa Usabiaga, E. Lushi, Y. Wu, L. Ristroph, J. Zhang, M. Ward, and M. J. Shelley, Relating Rheotaxis and Hydrodynamic Actuation using Asymmetric Gold-Platinum Phoretic Rods, Phys. Rev. Lett. **123**, 178004 (2019).

[15] R. Baker *et al.*, Fight the flow: the role of shear in artificial rheotaxis for individual and collective motion, Nanoscale **11**, 10944 (2019).

[16] L. D. Rubio, M. Potomkin, R. D. Baker, A. Sen, L. Berlyand, and I. S. Aranson, Self-propulsion and shear flow align active particles in nozzles and channels, Adv. Intell. Syst. **3**, 2000178 (2021).

[17] A. Zöttl and H. Stark, Nonlinear Dynamics of a Microswimmer in Poiseuille Flow, Phys. Rev. Lett. **108**, 218104 (2012).

[18] A. Zöttl and H. Stark, Periodic and quasiperiodic motion of an elongated microswimmer in Poiseuille flow, Eur. Phys. J. E **36**, 4 (2013).

[19] S. Uppaluri, N. Heddergott, E. Stellamanns, S. Herminghaus, A. Zöttl, H. Stark, M. Engstler, and T. Pfohl, Flow loading induces oscillatory trajectories in a bloodstream parasite, Biophys. J. **103**, 1162 (2012).

[20] S. Wang, H. Arellano-Santoyo, P. A. Combs, and J. W. Shaevitz, Actin-like cytoskeleton filaments contribute to cell mechanics in bacteria, Proc. Natl. Acad. Sci. U.S.A. **107**, 9182 (2010).

[21] Y. Caspi, Deformation of filamentous *Escherichia coli* cells in a microfluidic device: A new technique to study cell mechanics, PLoS One **9**, e83775 (2014).

[22] H. Wada and R. R. Netz, Model for Self-Propulsive Helical Filaments: Kink-Pair Propagation, Phys. Rev. Lett. **99**, 108102 (2007).

[23] M. Tournus, A. Kirshtein, L. V. Berlyand, and I. S. Aranson, Flexibility of bacterial flagella in external shear results in complex swimming trajectories, J. R. Soc. Interface **12**, 20140904 (2015).

[24] M. Kumar and A. M. Ardekani, Effect of external shear flow on sperm motility, Soft Matter **15**, 6269 (2019).

[25] M. Potomkin, M. Tournus, L. Berlyand, and I. S. Aranson, Flagella bending affects macroscopic properties of bacterial suspensions, J. R. Soc. Interface **14**, 20161031 (2017).

[26] A. Farutin, T. Piasecki, A. M. Słowicka, C. Misbah, E. Wajnryb, and M. L. Ekiel-Jeżewska, Dynamics of flexible fibers and vesicles in Poiseuille flow at low Reynolds number, Soft Matter **12**, 7307 (2016).

[27] A. M. Słowicka, E. Wajnryb, and M. L. Ekiel-Jeżewska, Lateral migration of flexible fibers in Poiseuille flow between two parallel planar solid walls, Eur. Phys. J. E **36**, 31 (2013).

[28] B. Kaoui, G. H. Ristow, I. Cantat, C. Misbah, and W. Zimmermann, Lateral migration of a two-dimensional vesicle in unbounded Poiseuille flow, Phys. Rev. E **77**, 021903 (2008).

[29] L. G. Leal, Particle motions in a viscous fluid, Annu. Rev. Fluid Mech. **12**, 435 (1980).

[30] M. Laumann, P. Bauknecht, S. Gekle, D. Kienle, and W. Zimmermann, Cross-stream migration of asymmetric particles driven by oscillating shear, Europhys. Lett. **117**, 44001 (2017).

[31] E. Wajnryb, K. A. Mizerski, P. J. Zuk, and P. Szymczak, Generalization of the Rotne–Prager–Yamakawa mobility and shear disturbance tensors, J. Fluid Mech. **731**, R3 (2013).

[32] P. J. Zuk, E. Wajnryb, K. A. Mizerski, and P. Szymczak, Rotne–Prager–Yamakawa approximation for different-sized particles in application to macromolecular bead models, J. Fluid Mech. **741**, R5 (2014).

[33] J. Hendricks, T. Kawakatsu, K. Kawasaki, and W. Zimmermann, Confined semiflexible polymer chains, Phys. Rev. E **51**, 2658 (1995).

[34] R. G. Winkler and G. Gompper, The physics of active polymers and filaments, J. Chem. Phys. **153**, 040901 (2020).

[35] A. Laskar and R. Adhikari, Brownian microhydrodynamics of active filaments, Soft Matter **11**, 9073 (2015).

[36] M. S. Rizvi, A. Farutin, and C. Misbah, Size and shape affect swimming of a triangular bead-spring microswimmer, Phys. Rev. E **98**, 043104 (2018).

[37] J. Elgeti, R. G. Winkler, and G. Gompper, Physics of microswimmers–single particle motion and collective behavior: a review, Rep. Prog. Phys. **78**, 056601 (2015).

[38] J. de Graaf, H. Menke, A. J. T. M. Mathijssen, M. Fabritius, C. Holm, and T. N. Shendruk, Lattice-Boltzmann hydrodynamics of anisotropic active matter, J. Chem. Phys. **144**, 134106 (2016).

[39] M. Laumann, W. Schmidt, A. Farutin, D. Kienle, S. Förster, C. Misbah, and W. Zimmermann, Emerging Attractor in Wavy Poiseuille Flows Triggers Sorting of Biological Cells, Phys. Rev. Lett. **122**, 128002 (2019).

[40] Simulation parameters for plane flows: time step $\Delta t = 0.01$, maximum flow speed $u_0 = 0.162$, channel half height $d = 20$, fluid viscosity $\eta = 1$, number of beads $N = 5$, equilibrium distance of two neighboring beads $b = 1.095$, bead radius $a = 0.5$ (aspect ratio $r_p = 5.38$, geometry factor $G = 0.933$), activity $F_0 = 0.6$ (intrinsic swimming speed $v_0 = 4.872 \times 10^{-3}$), harmonic spring stiffness $k = 10$, bending rigidity $\kappa = 0.5$, torque strength $\kappa_t = 10$, initial swimmer orientation $\psi_0 = \pm\pi$, and initial swimmer lateral position $y_0 = 5$. The migration direction is determined by the sign of the migration velocity which is obtained by a linear fit to $y_c(t)$ for $t \in [0, 10^5]$. Simulation parameters in wavy flows: activity $F_0 = 1$ (intrinsic swimming speed $v_0 = 0.0162$), bending rigidity $\kappa = 3$, dimensionless modulation amplitude $\varepsilon = 0.1$, modulation length $\lambda = 807$, initial swimmer orientation $\psi_0 = 0$, initial swimmer

position $(x_0, y_0) = (0, 1)$, and simulation time for each trajectory $t_{end} = 2 \times 10^6$. Remaining parameters as in simulations in plane flows.

[41] J. D. Weeks, D. Chandler, and H. C. Andersen, Role of repulsive forces in determining the equilibrium structure of simple liquids, J. Chem. Phys. **54**, 5237 (1971).

[42] L. Jibuti, L. Qi, C. Misbah, W. Zimmermann, S. Rafaï, and P. Peyla, Self-focusing and jet instability of a microswimmer suspension, Phys. Rev. E **90**, 063019 (2014).

[43] H.-C. Flemming, J. Wingender, U. Szewzyk, P. Steinberg, S. A. Rice, and S. Kjelleberg, Biofilms: an emergent form of bacterial life, Nat. Rev. Microbiol. **14**, 563 (2016).

[44] J. Hill, O. Kalkanci, J. L. McMurry, and H. Koser, Hydrodynamic Surface Interactions Enable *Escherichia Coli* to Seek Efficient Routes to Swim Upstream, Phys. Rev. Lett. **98**, 068101 (2007).

[45] T. Kaya and H. Koser, Direct upstream motility in Escherichia coli, Biophys. J. **102**, 1514 (2012).

[46] M. Michalska, F. Gambacorta, R. Divan, I. S. Aranson, A. Sokolov, P. Noirot, and P. D. Laible, Tuning antimicrobial properties of biomimetic nanopatterned surfaces, Nanoscale **10**, 6639 (2018).

[47] K. Vasilev, J. Cook, and H. J. Griesser, Antibacterial surfaces for biomedical devices, Expert Rev. Med. Devices **6**, 553 (2009).

[48] C. Kurzthaler and H. A. Stone, Microswimmers near corrugated, periodic surfaces, Soft Matter **17**, 3322 (2021).

[49] B. Ezhilan and D. Saintillan, Transport of a dilute active suspension in pressure-driven channel flow, J. Fluid Mech. **777**, 482 (2015).

[50] K. Qi, H. Annepu, G. Gompper, and R. G. Winkler, Rheotaxis of spheroidal squirmers in microchannel flow: Interplay of shape, hydrodynamics, active stress, and thermal fluctuations, Phys. Rev. Res. **2**, 033275 (2020).

[51] G. B. Jeffery, The motion of ellipsoidal particles immersed in a viscous fluid, Proc. Royal Soc. London A **102**, 161 (1922).

[52] M. S. Ingber and L. A. Mondy, A numerical study of three-dimensional Jeffery orbits in shear flow, J. Rheol. **38**, 1829 (1994).

[53] S. Tsangaris and E. Leiter, On laminar steady flow in sinusoidal channels, J. Eng. Math. **18**, 89 (1984).

[54] S. Tsangaris and D. Potamitis, On laminar small Reynolds-number flow over wavy walls, Acta Mech. **61**, 109 (1986).